## PAPER

Check for updates

# Temperature sensing in Tb3+/Eu3+-based tetranuclear silsesquioxane cages with tunable emission†

Karina Nigoghossian, [ID] *[a] Alena N. Kulakova,[bc] Gautier Félix, [ID] [a]
Victor N. Khrustalev,[cd] Elena S. Shubina, [ID] [b] Jérôme Long, [ID] [a] Yannick Guari, [ID] [a]
Saad Sene,[a] Luís D. Carlos, [ID] [e] Alexey N. Bilyachenko [ID] *[bc] and Joulia Larionova [ID] *[a]

New luminescent cage-like tetranuclear silsesquioxanes [NEt4][(Ph4Si4O8)2(Tb3Eu)(NO3)4(OH)(EtOH)3(H2O)]·4(EtOH) (**1**) and [NEt4]2[(Ph4Si4O8)2(Tb2Eu2)(NO3)6(EtOH)2(MeCN)2]·4(MeCN) (**2**) present a tunable thermosensitive Tb3+-to-Eu3+ energy transfer driven by Tb3+ and Eu3+ emission and may be used as temperature sensors operating in the range 41–100 °C with excellent linearity ($R^2 = 0.9990$) and repeatability (>95%). The thermometer performance was evidenced by the maximum relative sensitivity of 0.63% °C$^{-1}$ achieved at 68 °C.

## Introduction

Cage-like metallasilsesquioxanes (CLMSs) are an exciting family of molecule-based architectures of kaleidoscopic structural diversity built from metal ions or lanthanides and silsesquioxane ligands.[1,2] Their design benefits from both coordination and sol–gel chemistries, and for this reason these compounds are also described as hybrid organic–inorganic materials.[1,3] Indeed, the presence of silsesquioxanes, $(RSiO_{1.5})_n$ (where $n = 6$, 8, 10, 12, …), permits construction of inorganic Si–O–Si skeletons as a basic structural unit realizing cyclic and polycyclic types of matrixes, which offer to these architectures chemical stability, mechanical robustness, thermal stability, and the possibility to form a cage-like topology providing porosity and host–guest properties.[4] Moreover, these ligands can provide several modes of metal ion coordination, which explains the important diversity of structural arrangements of polyhedral cages, which can be designed in various shapes including adamantane, cooling tower, birdcage, cube, drum, sandwich-like, Asian lantern, and others.[1,2] On the other hand, the presence of various metal ions (for instance $Mg^{2+}$, $Ca^{2+}$, $Al^{3+}$, $Sn^{4+}$,

*etc.*), transition metal ions (such as $Pt^{2+/4+}$, $Cr^{3+}$, $Mn^{2+}$, $Ti^{3+}$, $Fe^{3+}$, $Ni^{2+}$, $Cu^{2+}$ or their combinations) or lanthanides (such as $Yb^{3+}$, $Nd^{3+}$, $Er^{3+}$, $Ce^{3+}$, $Eu^{3+}$, $Sm^{3+}$ or $Pr^{3+}$) usually situated in the core of CLMSs not only ensures the assembly of the whole architecture but also brings functional physical and chemical properties.[5] Among those, CLMSs have been widely investigated as molecule-based models for catalysis[6] or as a particular family of molecule-based magnets.[7] Unexpectedly, the optical properties of CLMSs have been investigated only scarcely. We can cite only one work reporting on luminescence in a mononuclear $Eu^{3+}$ based CLMS, but its crystal structure has not been clarified.[8] In this line of thought, we recently reported on the first series of luminescent tetranuclear lanthanide ions containing CLMSs presenting $Ln^{3+}$ characteristic emission and interesting magnetic properties.[9,10] However, the employment of CLMSs as temperature emissive sensors has never been reported up to now.

Indeed, accurate temperature measurements are an important issue for innovative technologies in a wide range of fields, including electronics, photonics, and biology. The conventional thermometers require close contact between the probe and the specimen, which hampers temperature sensing with high spatial resolution. Luminescent thermometry enables remote sensing by monitoring the emission of a probe.[11] Several types of luminescent materials can be used for temperature sensing, including $Ln^{3+}$-based complexes, semiconductor nanocrystals (quantum dots), and organic dyes.[11] The former allows designing thermometry self-referencing methods based on the luminescence intensity ratio (LIR) of two distinct $Ln^{3+}$ transitions,[12] which are not affected by variations in probe concentration, excitation power, detection system, and others.[11] Among them, materials based on a solid solution of $Eu^{3+}/Tb^{3+}$ materials have widely been proposed as temperature sensors[13–16] using the LIR between $Tb^{3+}$ green and $Eu^{3+}$ red emissions ($^5D_4 \rightarrow {}^7F_5$ and $^5D_0 \rightarrow {}^7F_2$ transitions, respectively). The nature of the host lattice and ligands highly affects the temperature dependence of both

[a]*ICGM, Univ. Montpellier, CNRS, ENSCM, Montpellier, France. E-mail: karina. nigoghossian@umontpellier.fr; joulia.larionova@umontpellier.fr*

[b]*Nesmeyanov Institute of Organoelement Compounds, Russian Academy of Sciences, Vavilova str., 28, Moscow, 119991, Russia. E-mail: bilyachenko@ineos.ac.ru*

[c]*Peoples' Friendship University of Russia (RUDN), Miklukho-Maklay Str., 6, Moscow, 117198, Russia*

[d]*Zelinsky Institute of Organic Chemistry, Russian Academy of Sciences, Leninsky Prospect 47, Moscow 119991, Russia*

[e]*Phantom-g, Physics Department and CICECO – Aveiro Institute of Materials, University of Aveiro, Aveiro, 3810-193, Portugal*

† Electronic supplementary information (ESI) available. CCDC 2094637 and 2002352. For ESI and crystallographic data in CIF or other electronic format see DOI: 10.1039/d1ra06755a

emissions. The ratiometric $Eu^{3+}/Tb^{3+}$ luminescent thermometers are designed from a simple physical mixture of mononuclear complexes of both $Ln^{3+}$ (ref. 13–16) or as a solid solution of mono or polynuclear complexes containing both $Ln^{3+}$ in the same compound.[17–19] In the latter case, the proximity of $Ln^{3+}$ emitting centers enables energy transfer (ET) among them, which affects the green-to-red LIR. Therefore, the thermometric parameter (LIR) can be adjusted by varying the $Ln^{3+}$ composition, and serve as an interesting strategy to optimize the thermometer performance.[19]

In this work, we report on tunable emission of tetranuclear CLMSs, linked to the $Tb^{3+}$-to-$Eu^{3+}$ energy transfer (ET), which may be used for temperature sensing. The investigation on the sensing properties reveals great stability and repeatability after multiple heating/cooling cycles. This important stability to photobleaching and a relatively high working temperature (to 100 °C) are ensured by the presence of a siloxane matrix, which plays a protective role.

## Results and discussion

The synthesis of $[NEt_4][(Ph_4Si_4O_8)_2(Tb_3Eu)(NO_3)_4(OH)(EtOH)_3(H_2O)]\cdot$ $4(EtOH)$ **1** and $[NEt_4]_2[(Ph_4Si_4O_8)_2(Tb_2Eu_2)(NO_3)_6(EtOH)_2(MeCN)_2]\cdot$ $4(MeCN)$ **2** compounds has been performed by adapting the previously described procedure consisting in a two-step reaction involving, first: the *in situ* formation of phenylsiloxanolate $[PhSi(O)ONa]_x$ species with their following self-assembling reaction with $Et_4NCl$ and the corresponding $Tb^{3+}$ and $Eu^{3+}$ salts with the $Tb^{3+}/Eu^{3+}$ ratio equal to 3/1 for **1** and 2/2 for **2**, respectively. X-ray diffraction analysis performed on single crystals of **1** and **2** indicates that these compounds crystalize in the $P\bar{1}$ space group (Table S1, ESI†). The crystal structure of **2** is similar to those previously published pure Eu and Tb analogues.[9]

Briefly, the molecular structure may be described as a $(Tb_{1-x}Eu_xO_2)_4$ core (where $x = 0.25$ for **1** and 0.50 for **2**) caught between two tetraphenylcyclotetrasiloxanolates and assembled in a prism-like polyhedron (Fig. 1, S1, S3 and S4, ESI†). The cores are constituted by four statistically distributed Tb/Eu ions linked through oxygen atoms forming a distorted square. In both compounds, there are two different eight coordinated Tb/Eu sites, which adopt a distorted square antiprism geometry. Each lanthanide ion in **1** is coordinated by four bridging oxygens and three oxygens from terminal nitrate and ethanol. The tetranuclear cycle encapsulates also an hydroxyl group situated in the centre. In **2**, one lanthanide site is coordinated by four bridging oxygen atoms and four oxygen atoms from two terminal nitrate ligands, while another is linked to four bridging oxygens, three oxygens from one terminal nitrate, and one ethanol and nitrogen from acetonitrile. The main distances and angles are given in ESI (Table S2†). The anionic CLMS molecules are aligned along the $b$ axis and alternated with $Et_4N^+$ cations (Fig. S2 and S5, ESI†). The atomic Tb/Eu ratio determined by SEM-EDX is equal to 3 : 1 and 1 : 1 for **1** and **2**, respectively, confirming the expected Tb/Eu ratio in the core of CLMSs (Table S3, ESI†). The thermogravimetric analysis indicates that the complexes **1** and **2** start to decompose from 240 °C (Fig. S6, ESI†).

The morphological characterisations have been performed by Scanning Electronic Microscopy (SEM), which indicates the
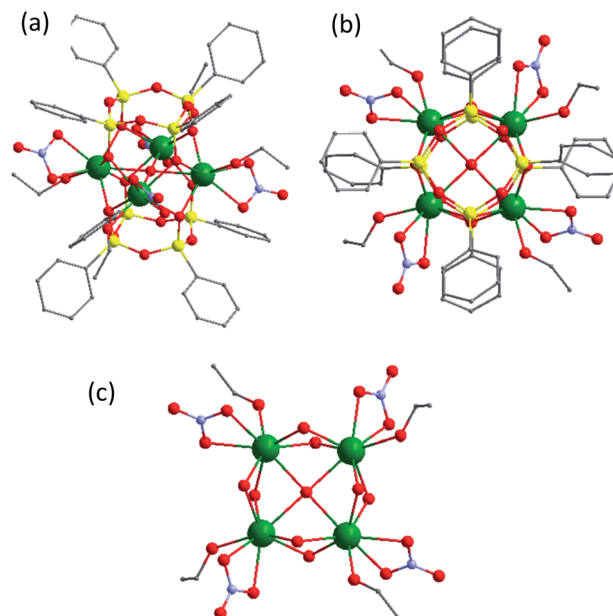


Fig. 1 Two different views of molecular structure of **1** (a) and (b). Hydrogen atoms and crystallized ethanol molecules have been omitted for clarity; (c) representation $(Tb_{0.75}Eu_{0.25}O_2)_4O$ core of **1** showing the coordination geometry of Tb/Eu sites. Color code: green Tb/Eu; yellow Si; red O; blue N; grey C.

presence of microparticles in samples (Fig. 2 and S7, ESI†). The profile curve permitting to probe the chemical analysis indicates the homogeneity of sample.

The magnetic measurements performed for both compounds are perfectly coherent with the presence of 75 and 50% occupation of $Tb^{3+}$ ions $(^7F_6, S = 3, L = 3, g = 3/2, \chi T = 11.82$ cm$^3$ K mol$^{-1})$ for **1** and **2**, respectively, since $Eu^{3+}$ is diamagnetic (Fig. S8, ESI†).

The photoluminescence of CLMSs in the solid-state was first investigated at room temperature. The excitation spectra of **1** were recorded by monitoring the main emissions of $Eu^{3+}$ at
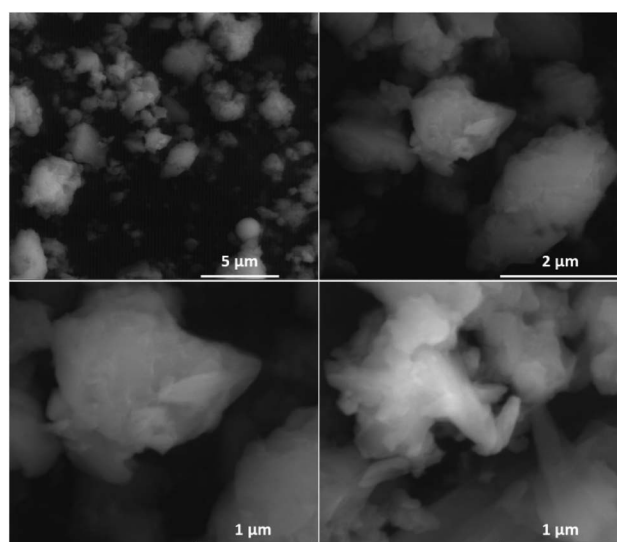


Fig. 2 SEM images for sample **1** with different magnifications.

612 nm ($^5D_0 \rightarrow {}^7F_2$) and Tb$^{3+}$ at 543 nm ($^5D_4 \rightarrow {}^7F_5$) (Fig. 3a). The diverse observed lines are assigned to intra-4f transitions of Eu$^{3+}$ (ref. 20) and Tb$^{3+}$.[21] Its luminescence properties are similar to those of previously published single Eu$^{3+}$ or Tb$^{3+}$ containing CLMSs.[9] The maximum intensity of excitation for Eu$^{3+}$ red emission is located at 394 nm, which corresponds to the Eu$^{3+}$ transition $^7F_0 \rightarrow {}^5L_6$. As for Tb$^{3+}$ green emission, the highest excitation intensity is observed at 378 nm, which is attributed to the transition $^7F_6 \rightarrow {}^5G_6, {}^5D_3$. The Tb$^{3+}$-to-Eu$^{3+}$ ET is evidenced by the presence of the Tb$^{3+}$ transition lines in the excitation spectra monitored in the Eu$^{3+}$ emission (at 612 nm).

The emission spectra of **1** were measured under excitation at 394 nm and 378 nm (Fig. 3b). Upon 394 nm irradiation, the Eu$^{3+}$ ion is selectively excited to the $^5L_6$ energy level, and, subsequently, non-radiative relaxations lead to the population of the $^5D_0$ emitting state. The Eu$^{3+}$ transitions are then observed from $^5D_0$ to $^7F_J$ ($J = 0$–4) manifold. The excitation at a higher energy state, under 378 nm irradiation, leads to the emissions of Tb$^{3+}$ from $^5D_4$ to $^7F_J$ ($J = 6$–2) manifold, as well as Eu$^{3+}$ transitions ($^5D_0 \rightarrow {}^7F_J$, $J = 0$–4). This result indicates an intramolecular Tb$^{3+}$-to-Eu$^{3+}$ ET considering the relatively short distances between lanthanides in the CLMS core (the shortest direct Ln$^{3+}$–Ln$^{3+}$ distance in **1** is 3.5087 Å and the shortest Ln$^{3+}$–Ln$^{3+}$ distance through the bridging oxygen atom is 4.6616 Å, Table S2 and Fig. S1, ESI†).[22] Furthermore, the observation of the very weak transition $^5D_0 \rightarrow {}^7F_0$ at 579 nm visible in both emission spectra (insets of Fig. 3b), indicates low symmetry of the Eu$^{3+}$

coordination environment. The presence of one sharp peak at this region suggests rather a single chemical environment.[23]

The excitation and emission spectra of **2** show some differences in comparison with **1** (Fig. S9, ESI†). In particular, the emission spectrum under excitation at 378 nm exhibits lower green-to-red (543 to 612 nm) LIR in comparison with **1**. The relative higher red emission at lower Eu$^{3+}$ amount for **1** also suggests that the intramolecular Tb$^{3+}$-to-Eu$^{3+}$ ET occurs to the detriment of Tb$^{3+}$ emission $^5D_4 \rightarrow {}^7F_5$ (543 nm), which is in agreement with the literature.[17,19]

The Tb$^{3+}$-to-Eu$^{3+}$ ET has previously been reported in inorganic[24,25] and molecular luminescent materials.[17,26–28] Its occurrence and its efficiency highly depends on the crystal structure, the presence of relatively short intra or intermolecular Tb$^{3+}$...Eu$^{3+}$ distances and/or the nature of ligands.[27] Indeed, the efficient Tb$^{3+}$-to-Eu$^{3+}$ ET occurred under direct excitation of Tb$^{3+}$ (ref. 26) or through an antenna effect in Eu$^{3+}$/Tb$^{3+}$ coordination polymers having relatively short intramolecular distances between lanthanide ions.[28] Alternatively, in coordination polymers built from Tb$^{3+}$ and Eu$^{3+}$ β-diketone complexes linked through a bridging phosphine oxide the presence of organic bridging ligands allowed the ET to occur despite the long distances between the lanthanides (13.6 Å). In fact, the Tb$^{3+}$-to-Eu$^{3+}$ ET rates depends on the operative multipolar and exchange mechanisms that are a function of the distance between the two ions ($R_L$). While for the former, the electric dipole-electric dipole, electric dipole-electric
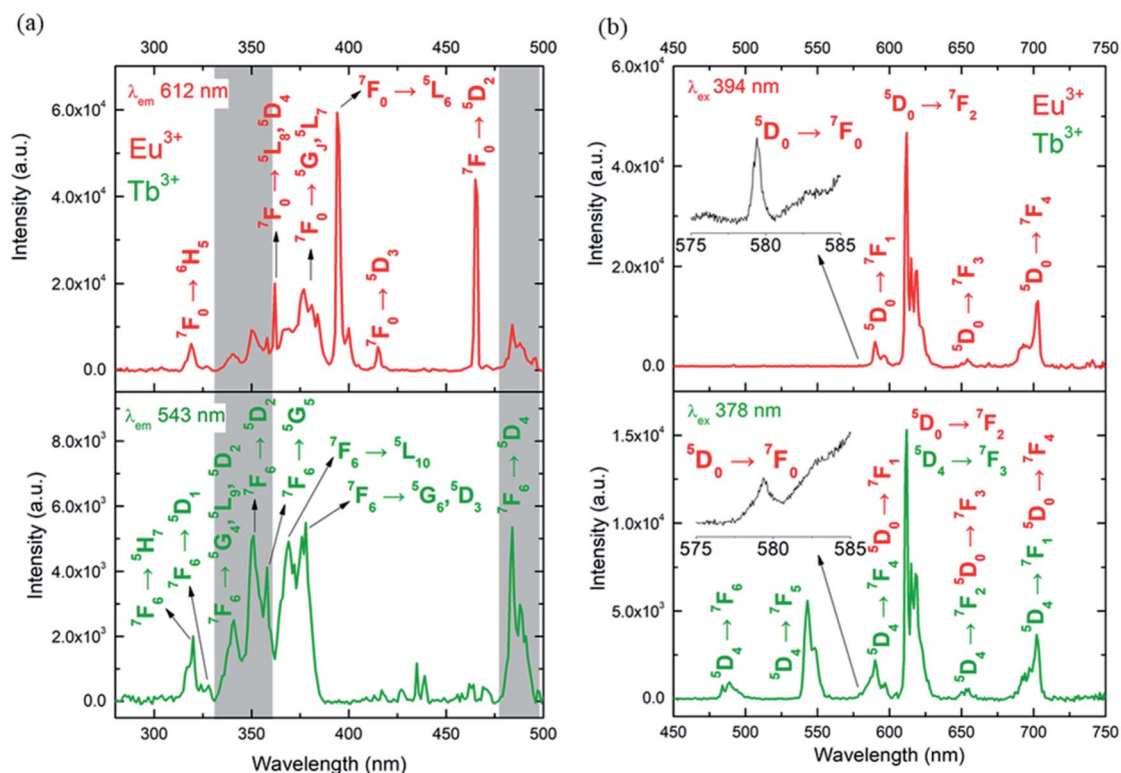


**Fig. 3** Room temperature (a) excitation spectra of **1** monitored at $\lambda_{em} = 612$ (top) and $\lambda_{em} = 543$ nm (bottom), and (b) emission spectra of **1** performed with $\lambda_{ex} = 394$ (top) and $\lambda_{ex} = 398$ nm (bottom). Eu$^{3+}$ and Tb$^{3+}$ transitions are written in red and green, respectively. Inserts: high-resolution emission spectra for the $^5D_0 \rightarrow {}^7F_0$ transition.

quadrupole, and electric quadrupole-electric quadrupole rates depend on $R_L^{-6}$, $R_L^{-8}$ and $R_L^{-10}$, respectively, the exchange transfer rate decreases exponentially with increasing $R_L$. In this later case, the exchange mechanism becomes significant for $Tb^{3+}$-to-$Eu^{3+}$ separations lower than 4 Å.[22]

In order to confirm the presence of an intramolecular $Tb^{3+}$-to-$Eu^{3+}$ ET in **1** and **2**, the luminescence of a physical 3 : 1 mixture of powders of two previously published $(Et_4N)_2[(PhSiO_2)_8Tb_4(NO_3)_6(EtOH)_2(MeCN)_2]$ and $(Et_4N)_2[(PhSiO_2)_8Eu_4(NO_3)_6(EtOH)_2(MeCN)_2]$[9] was investigated (ratio Tb : Eu = 3 : 1, as confirmed by SEM-EDX, Table S3, ESI†). The excitation spectra (Fig. S10a, ESI†) monitored for $Eu^{3+}$ red emission (612 nm) and $Tb^{3+}$ green emission (at 543 nm) have a similar profile as observed for **1**. The emission spectra under 394 and 378 nm are presented on Fig. S10b, ESI.† Under 394 nm-excitation, the expected $Eu^{3+}$ transitions are observed ($^5D_0 \rightarrow {}^7F_{0-4}$). The excitation at 378 nm leads mainly to $Tb^{3+}$ emissions, while some low intensity $Eu^{3+}$ emission bands can also be detected due to the less-efficient intermolecular ET. This fact reinforces the evidence of an intramolecular ET in **1** and **2** occurring due to the short distances between the donor ($Tb^{3+}$) and the acceptor ($Eu^{3+}$) ions.[22] Therefore, the emissive levels of $Tb^{3+}$ and $Eu^{3+}$ ($^5D_4$ and $^5D_0$, respectively) are close enough in energy, thus permitting this $Tb^{3+}$-to-$Eu^{3+}$ ET. The observation of $Eu^{3+}$ red emission (at ~612 nm) *via* $Tb^{3+}$ excitation (at ~350–380 nm), where the $Eu^{3+}$ emission occurs to the detriment of the $Tb^{3+}$ radiative decay, clearly proves this fact. In order to investigate the possibility to use our CLMSs as emissive thermometers, the luminescence has been investigated at different temperatures. Fig. 4 shows the spectra of **1** measured under 365 nm excitation from 40 to 100 °C, and the corresponding LIR between $Tb^{3+}$ and $Eu^{3+}$ emissions (at 543 nm and 612 nm, respectively). The wavelength ranges used to compute the integrated areas are 530–565 nm ($Tb^{3+}$: $^5D_4 \rightarrow {}^7F_5$) and 603–637 nm ($Eu^{3+}$: $^5D_0 \rightarrow {}^7F_2$). The error bars represent the standard deviation of average values obtained upon three consecutive temperature cycles (Fig. S11, ESI†). The temperature-dependent variation of the parameter LIR ($I_{543}/I_{612}$) shows a linear correlation, indicative of a self-referencing temperature sensor. The calibration parameters are presented in Table S4 (ESI†) along with several metric parameters that provide the thermometric performance in the operating temperature range. The regression coefficient ($R^2$) revealed an excellent calibration linearity ($R^2 = 0.9990$) in the temperature range 41–100 °C. We also verified the repeatability, which corresponds to the variability among the measurements, which is indicated by the relative standard deviation (RSD). Therefore, satisfactory repeatability was observed as the maximum RSD among measurements values was lower than 5%. The relative thermal sensitivity ($S_r$) is the parameter that allows the comparison of thermometric performance among different types of thermometers.[29,30] The $S_r$ represents the variation of the experimental parameter (LIR in the present case) per degree of temperature, expressed as:

$$S_r(T) = |\partial LIR(T)/\partial T|/LIR(T).$$

The maximum $S_r$ value estimated from the calibration data was found to be 0.63% °C$^{-1}$ at 68 °C, which is close to a frequently considered high relative thermal sensitivity (~1% °C$^{-1}$),[31] and in proximity with $S_r$ values reported for mixed $Eu^{3+}$/$Tb^{3+}$ compounds.[19] Temperature uncertainty (or thermal resolution, $\delta T$) is the smallest temperature change that can be detected.[31] This value is related to $S_r$ as follows:

$$\delta T = |\delta LIR(T)/LIR(T)|/S_r(T),$$

where $\delta LIR(T)$ is the standard deviation in the LIR($T$) obtained upon several heating cycles. According to this, the minimal thermal resolution is 0.04 °C. Therefore, the temperature sensor proposed here works reliably in temperature operating range 41–100 °C. Note that the $Tb^{3+}$ emission intensity decreased around 20% of its initial value upon temperature increase (Fig. S11, ESI†). On the other hand, the $Eu^{3+}$ transition showed an increase of about 10% of its initial value.

Compound **2** also shows the features making it interesting as self-referencing temperature sensor (Fig. S12, ESI†), but with lower sensitivity (Table S4, ESI†).

The thermal behavior of the emission spectra of CLMSs containing only $Eu^{3+}$ ($(Et_4N)_2[(PhSiO_2)_8Eu_4(NO_3)_6(EtOH)_2(MeCN)_2]$) or
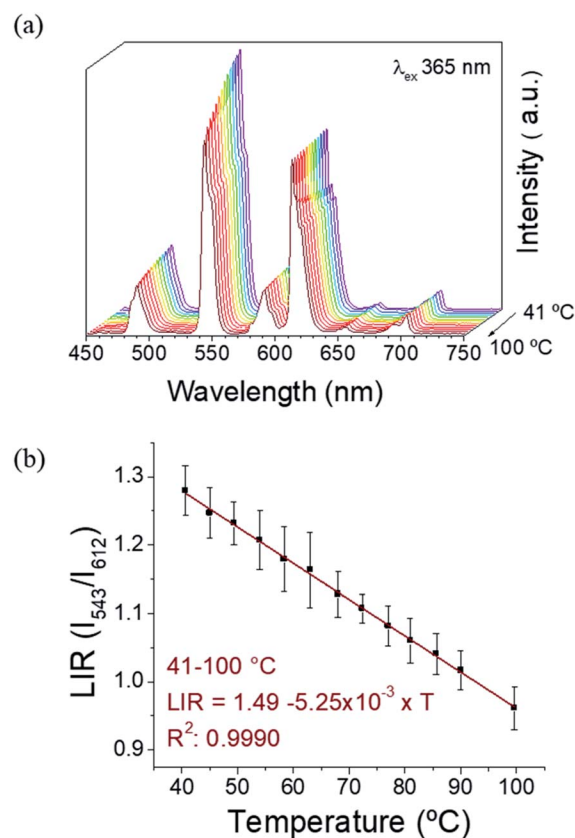


Fig. 4 (a) Emission spectra ($\lambda_{ex}$ = 365 nm) of **1** at different temperatures; and (b) corresponding LIR between the emissions at 543 nm and 612 nm. The solid line represents a linear fitting. Integrated areas: 530–565 nm ($Tb^{3+}$: $^5D_4 \rightarrow {}^7F_5$) and 603–637 nm ($Eu^{3+}$: $^5D_0 \rightarrow {}^7F_2$). The error bars correspond to standard error of mean determined from three consecutive temperature cycles.

$Tb^{3+}$ (($Et_4N$)$_2$[(PhSiO$_2$)$_8$Tb$_4$(NO$_3$)$_6$(EtOH)$_2$(MeCN)$_2$]) in the same temperature range is shown in Fig. S13 and S14 (ESI†), respectively. The slight decrease in $Tb^{3+}$ emission intensity with temperature (Fig. S14†) is related to the increase of nonradiative energy transfer from the $Tb^{3+}$ ion to the ligands to the detriment of the radiative emission. The thermal effect on $Tb^{3+}$ emission observed for **1** in the presence of $Eu^{3+}$ suggests an additional energy transfer pathway among emitting centers probably arising due to the presence of the hydroxyl bridge in the center of the cage **1** and also due to the shorter intermolecular Tb/Eu···Tb/Eu distances (see Fig. S1 and S4, ESI†). As the thermal effect on $Tb^{3+}$ emission is more relevant in the presence of $Eu^{3+}$, we consider that the ET $Tb^{3+} \rightarrow Eu^{3+}$ has improved the thermal sensitivity of $Tb^{3+}$ emission, and therefore enabled the application of the heteronuclear $Tb^{3+}$/$Eu^{3+}$ CLMSs for luminescent thermometry.[19]

## Conclusions

In summary, two tetranuclear $Tb^{3+}$/$Eu^{3+}$ based silsesquioxane cages with a prism-like topology have been synthesized and characterized. The morphological characterisations performed by means of SEM indicate the presence of microparticles in samples as well as their homogeneity. The compounds exhibit the terbium and europium characteristic green and red emissions. The relatively short intramolecular distances between the lanthanide atoms in the cores of CLMSs have enabled the intramolecular $Tb^{3+}$-to-$Eu^{3+}$ energy transfer, as evidenced by the europium emissions observed under excitation in the terbium-excited levels. The tetranuclear structure has enabled the design of the compounds with well-defined $Eu^{3+}$ and $Tb^{3+}$ molar ratio, and therefore the control of the intrametallic interactions. The relative intensity of the red $Eu^{3+}$ emission ($^5D_0 \rightarrow {}^7F_2$) increases along with the relative amount of the $Eu^{3+}$ with respect to the green $Tb^{3+}$ one ($^5D_4 \rightarrow {}^7F_5$) because of the increased ET effect. In this sense, a better thermal sensitivity in **1** in comparison with **2** can be attributed to its lower relative intensity of $Eu^{3+}$ red emission. On the other hand, the thermal sensitivity of $Tb^{3+}$ emission increased in the presence of $Eu^{3+}$ in the heteronuclear CLMSs in comparison with the homonuclear $Tb^{3+}$-based one, because of the occurrence of an additional nonradiative ET pathway. The $Tb^{3+}$/$Eu^{3+}$-based CLMSs were then proposed as self-referenced temperature sensors based on the LIR of $Tb^{3+}$ and $Eu^{3+}$ transitions ($^5D_4 \rightarrow {}^7F_5$ and $^5D_0 \rightarrow {}^7F_2$). The sensor **1** showed an excellent linearity in the temperature range 41–100 °C with the maximum relative thermal sensitivity of 0.63% °C$^{-1}$ at 68 °C, which indicates its successful performance. Its important stability to photobleaching at a relatively high working temperature (100 °C) is certainly due to the presence of the siloxane matrix, which plays a protective role. This work opens great perspectives for the design of new class of CLMSs-based temperature sensors.

## Experimental procedures

### Materials

Phenyltrimethoxysilane (98%), $Et_4NCl$ ($\geq$98%), $Eu(NO_3)_3 \cdot 6H_2O$ (99.9% trace metals basis), $Tb(NO_3)_3 \cdot 6H_2O$ (99.9% trace metals basis), ethanol and acetonitrile were purchased from Merck and used as received.

### Synthesis

The synthesis of compounds **1** and **2** has been performed in a similar way. A mixture of PhSi(OMe)$_3$ and NaOH was dissolved in 30 mL of ethanol. The resulting solution was heated to reflux for 1.0 h. Afterwards the mixture of $Tb(NO_3)_3 \cdot 6H_2O$ and $Eu(NO_3)_3 \cdot 6H_2O$ in proportions 3/1 for **1** and 2/2 for **2** and $Et_4NCl$ dissolved in 30 mL of $CH_3CN$ were added at once. The resulted mixture was heated to reflux for 3 h. Filtration of the mixture from the insoluble part gave a non-colored solution. Slow evaporation of solvents (ethanol/$CH_3CN$) gave in a period of 5–10 days a bunch of crystalline material. The single crystals suitable for a single crystal X-ray diffraction were collected. The crystal products were dried in vacuum to perform elemental analysis and to calculate the yield.

**Compound ($Et_4N$)[(PhSiO$_{1.5}$)$_8$(Tb$_{0.75}$Eu$_{0.25}$O$_{1.5}$)$_4$(O)(NO$_{2.5}$)$_4$(-EtOH)$_4$] (1).** Reactants loadings: PhSi(OMe)$_3$ (0.186 g, 0.8 mmol), NaOH (0.032 g, 0.8 mmol), $Tb(NO_3)_3 \cdot 6H_2O$ (0.131 g, 0.3 mmol), $Eu(NO_3)_3 \cdot 6H_2O$ (0.045 g, 0.1 mmol), $Et_4NCl$ (0.066 g, 0.4 mmol). Yield = 38.24% (0.87 g).

Anal. calcd for $C_{62}H_{81}N_5O_{33}Si_8Tb_3Eu$: % C 32.69, % H 3.58, % N 3.07. Found: % C 29.68, % H 3.39, % N 3.01. IR in KBr pellets (cm$^{-1}$): 3448 (w), 3073 (s), 3050 (s), 3005 (s), 1624 (w), 1593 (s), 1500 (w), 1430 (s), 1384 (s), 1314 (w), 1129 (s), 1027 (m), 997 (s), 945 (w), 813 (s), 785 (s), 747 (s), 705 (s), 678 (s), 646 (s), 576 (s), 548 (s), 499 (s), 467 (s).

Scanning Electronic Microscopy (SEM) image is shown in Fig. S14 (ESI†).

**Compound ($Et_4N$)$_2$[(PhSiO$_{1.5}$)$_8$(Tb$_{0.5}$Eu$_{0.5}$O$_{1.5}$)$_4$(O)(NO$_{2.5}$)$_6$(EtOH)$_2$(MeCN)$_2$] (2).** Reactants loadings: PhSi(OMe)$_3$ (0.186 g, 0.8 mmol), NaOH (0.032 g, 0.8 mmol), $Tb(NO_3)_3 \cdot 6H_2O$ (0.091 g, 0.2 mmol), $Eu(NO_3)_3 \cdot 6H_2O$ (0.089 g, 0.2 mmol), $Et_4NCl$ (0.066 g, 0.4 mmol). Yield = 25.83% (0.34 g).

Anal. calcd for $C_{72}H_{98}N_{10}O_{36}Si_8Tb_2Eu_2$: % C 34.23, % H 3.91, % N 5.54. Found: % C 33.72, % H 3.83, % N 5.29. IR in KBr pellets (cm$^{-1}$): 3437 (w), 3484 (w), 3074 (s), 1617 (w), 1593 (s), 1500 (w), 1430 (s), 1384 (s), 1316 (s), 1129 (s), 1058 (m), 997 (s), 950 (w), 746 (s), 704 (s), 678 (s), 576 (s), 497 (s), 467 (s).

### Characterizations

Morphological characterizations and quantifications of Eu, Tb and Si elements were performed by using Scanning electron microscope and Energy Dispersive X-ray Analysis (SEM-EDX) on a FEI Quanta FEG 200 instrument. The powders were deposited on an adhesive carbon film and analyzed under vacuum. The quantification of the heavy elements was carried out with the INCA software, with a dwell time of 3 μs. IR spectra (KBr pellets) were recorded using PerkinElmer Spectrum Two FT-IR Spectrometer. The N, C, H elemental analyses were carried out in the microanalytical laboratory of the IOC RAS (Moscow) by means of a Carlo Erba Model 1106 elemental analyzer with an accepted tolerance of 0.4 unit on carbon (C), hydrogen (H), and nitrogen (N).

The emission and excitation spectra were at first evaluated at room (298 K) and low (77 K) temperatures using a spectrofluorimeter Edinburgh FLS-920. The excitation source was a 450 W Xe arc lamp. The spectra were corrected for detection and

optical spectral response of the spectrofluorimeter. In the second step, the emission spectra were measured as a function of temperature. The temperature setup included a thermal element (Heidolph, MR Hei-Tec (EU), 825 W, plate diameter 145 mm), a thermal camera (Optris PI 450i, accuracy $\pm$ 0.01 °C), an excitation source and a detector. The powder sample was placed on a cover glass (14 mm dia.) at the center of the heating source. The thermal camera was positioned at an angle of 30° relative to the sample to work as a temperature standard controller. A UV LED operating at 365 nm (ThorLabs M365L2) was used to excite the samples ($I$ = 0.7 A) by irradiating at a distance of 15 mm from the sample surface. The spectrometric detector and the excitation source were coupled by using a multimode fiber. The fiber excitation output and detector were located at the top of sample. A long pass filter (in-line fiber optic filter mount, ThorLabs FOFMS/M, 450 nm, 20 μm) was placed in light path between sample and detector to avoid artefacts arising from excitation source. The emission spectra were recorded in the temperature range from 20 to 110 °C. At each temperature step, a period of 10 min was given to allow the temperature to stabilize, and then 10 emission spectra were recorded from an average of 10 consecutive spectra with an integration time of 100 ms.

UV-visible-NIR absorption spectrum was measured using a spectrophotometer Specord 210 Plus (Analytik Jena AG, Germany).

Magnetic susceptibility data were collected with a Quantum Design MPMS-XL SQUID magnetometer working between 1.8–350 K with the magnetic field up to 7 Tesla. The sample was prepared in an ambient condition. The data were corrected for the sample holder and the diamagnetic contributions calculated from the Pascal's constants.

## Conflicts of interest

There are no conflicts to declare.

## Acknowledgements

## References

1 H. W. Roesky, G. Anantharaman, V. Chandrasekhar, V. Jancik and S. Singh, *Chem.-Eur J.*, 2004, **10**, 4106.

2 V. Lorenz and F. T. Edelmann, *Adv. Organomet. Chem.*, 2005, **53**, 101; M. M. Levitsky, B. G. Zavin and A. N. Bilyachenko, *Russ. Chem. Rev.*, 2007, **76**, 847; M. M. Levitsky and A. N. Bilyachenko, *Coord. Chem. Rev.*, 2016, **306**, 235.

3 R. Murugavel, A. Voigt, M. G. Walawalkar and H. W. Roesky, *Chem. Rev.*, 1996, **96**, 2205–2236.

4 R. Duchateau, *Chem. Rev.*, 2002, **102**, 3525; M. M. Levitsky, Y. V. Zubavichus, A. A. Korlyukov, V. N. Khrustalev, E. S. Shubina and A. N. Bilyachenko, *J. Clust. Sci.*, 2019, **30**, 1283.

5 F. Edelmann, P. Jutzi and U. Schubert, *Silicon Chemistry: From the Atom to Extended Systems*, ed. P. Jutzi and U. Schubert, 2007, p. 383; K. Sheng, Y.-N. Liu, R. K. Gupta, M. Kurmoo and D. Sun, *Sci. China: Chem.*, 2021, **64**, 419.

6 M. Levitskii, V. Smirnov, B. Zavin, A. Bilyachenko and A. Y. Rabkina, *Kinet. Catal.*, 2009, **50**, 490; E. A. Quadrelli and J.-M. Basset, *Coord. Chem. Rev.*, 2010, **254**, 707; K. Wada and T.-A. Mitsudo, *Catal. Surv. Asia*, 2005, **9**, 229; M. M. Levitsky, A. N. Bilyachenko and G. B. Shul'pin, *J. Organomet. Chem.*, 2017, **849–850**, 201; M. M. Levitsky, A. I. Yalymov, A. N. Kulakova, A. A. Petrov and A. N. Bilyachenko, *J. Mol. Catal. A: Chem.*, 2017, **426**, 297.

7 M. M. Levitsky, A. N. Bilyachenko, E. S. Shubina, J. Long, Y. Guari and J. Larionova, *Coord. Chem. Rev.*, 2019, **398**, 213015.

8 S. Marchesi, F. Carniato and E. Boccaleri, *New J. Chem.*, 2014, **38**, 2480.

9 A. N. Kulakova, A. N. Bilyachenko, M. M. Levitsky, V. N. Khrustalev, E. S. Shubina, G. Félix, E. Mamontova, J. Long, Y. Guari and J. Larionova, *Chem.-Eur. J.*, 2020, **26**, 16594.

10 A. N. Kulakova, K. Nigoghossian, G. Félix, V. N. Khrustalev, E. S. Shubina, J. Long, Y. Guari, L. D. Carlos, A. N. Bilyachenko and J. Larionova, *Eur. J. Inorg. Chem.*, 2021, (27), 2696–2701.

11 C. D. S. Brites, P. P. Lima, N. J. O. Silva, A. Millán, V. S. Amaral, F. Palacio and L. D. Carlos, *Nanoscale*, 2012, **4**, 4799.

12 C. D. S. Brites, S. Balabhadra and L. D. Carlos, *Adv. Opt. Mater.*, 2019, **7**, 1801239.

13 R. Piñol, C. D. S. Brites, R. Bustamante, A. Martínez, N. J. O. Silva, J. L. Murillo, R. Cases, J. Carrey, C. Estepa, C. Sosa, F. Palacio, L. D. Carlos and A. Millán, *ACS Nano*, 2015, **9**, 3134; A. M. Kaczmarek, D. Esquivel, B. Laforce, L. Vincze, P. Van Der Voort, F. J. Romero-Salguero and R. Van Deun, *Luminescence*, 2018, **33**, 567.

14 L. B. Guimarães, A. M. P. Botas, M. C. F. C. Felinto, R. A. S. Ferreira, L. D. Carlos, O. L. Malta and H. F. Brito, *Materials Advances*, 2020, **1**, 1988.

15 C. D. S. Brites, P. P. Lima, N. J. O. Silva, A. Millán, V. S. Amaral, F. Palacio and L. D. Carlos, *Adv. Mater.*, 2010, **22**, 4499.

16 C. J. Salas-Juárez, R. E. Navarro, A. Pérez-Rodríguez, U. Orozco-Valencia and R. Acevesm, *Sens. Actuators, A*, 2020, **315**, 112293.

17 M. Hatanaka, Y. Hirai, Y. Kitagawa, T. Nakanishi, Y. Hasegawa and K. Morokuma, *Chem. Sci.*, 2017, **8**, 423.

18 Y. Cui, H. Xu, Y. Yue, Z. Guo, J. Yu, Z. Chen, J. Gao, Y. Yang, G. Qian and B. Chen, *J. Am. Chem. Soc.*, 2012, **134**(9), 3979.

19 V. Trannoy, A. N. Carneiro Neto, C. D. S. Brites, L. D. Carlos and H. Serier-Brault, *Adv. Optical Mater.*, 2021, **9**, 2001938.

20 W. T. Carnall, P. R. Fields and K. Rajnak, *J. Chem. Phys.*, 1968, **49**, 4450.

21 W. T. Carnall, P. R. Fields and K. Rajnak, *J. Chem. Phys.*, 1968, **49**, 4447.

22 O. L. Malta, *J. Non-Cryst. Solids*, 2008, **354**, 4770; A. N. Carneiro Neto, R. T. Moura, A. Shyichuk, V. Paterlini, F. Piccinelli, M. Bettinelli and O. L. Malta, *J. Phys. Chem. C*, 2020, **124**, 10105; P. A. Tanner, L. Zhou, C. Duan and K.-L. Wong, *Chem. Soc. Rev.*, 2018, **47**, 5234; D. L. Dexter and J. H. Schulman, *J. Chem. Phys.*, 1954, **22**, 1063; G. Blasse and B. C. Grabmaier. *Luminescent materials*, Springer, Berlin, 1994.

23 J. Kai, D. F. Parra and H. F. Brito, *J. Mater. Chem.*, 2008, **18**, 4549.

24 V. Khudoleeva, L. Tcelykh, A. Kovalenko, A. Kalyakina, A. Goloveshkin, L. Lepnev and V. Utochnikova, *J. Lumin.*, 2018, **201**, 500.

25 T. Li, P. Li, Z. Wang, S. Xu, Q. Bai and Z. Yang, *Dalton Trans.*, 2015, **44**, 16840; M. Jiao, N. Guo, W. Lü, Y. Jia, W. Lv, Q. Zhao, B. Shao and H. You, *Dalton Trans.*, 2013, **42**, 12395; T. K. Anh, T. Ngoc, P. T. Nga, V. T. Bitch, P. Long and W. Stręk, *J. Lumin.*, 1988, **39**, 215.

26 E. Chelebaeva, J. Long, J. Larionova, R. A. S. Ferreira, L. D. Carlos, F. A. Almeida Paz, J. B. R. Gomes, A. Trifonov, C. Guérin and Y. Guari, *Inorg. Chem.*, 2012, **51**, 9005.

27 C. Piguet, J. C. G. Bünzli, G. Bernardinelli, G. Hopfgartner and A. F. Williams, *J. Am. Chem. Soc.*, 1993, **115**, 8197.

28 A. R. Ramya, D. Sharma, S. Natarajan and M. L. P. Reddy, *Inorg. Chem.*, 2012, **51**, 8818.

29 *Thermometry at the Nanoscale*, ed. L. D. Carlos and F. Palacio, Nanoscience & Nanotechnology Series, 2015.

30 A. Bednarkiewicz, L. Marciniak, L. D. Carlos and D. Jaque, *Nanoscale*, 2020, **12**, 14405.

31 C. D. S. Brites, A. Millán, and L. D. Carlos, In *Handbook on the Physics and Chemistry of Rare Earths*, ed. J. C. G. Bünzli and V. K. Pecharsky, Elsevier B.V., Amsterdam, 2016, vol. 49, p. 339.